

**PHASE TRANSFORMATION IN AMMONIUM SULFATE AEROSOLS:
DATA AND MODEL COMPARISON**

Dan Imre, Jun Xu, Robert McGraw, and Ignatius Tang

Abstract

The complete temperature dependent phase diagrams of the binary $(\text{NH}_4)_2\text{SO}_4/\text{H}_2\text{O}$ system are derived from data collected in a low temperature single levitated particle apparatus. The conditions of vapor pressure, temperature, and composition at which particle phase transitions take place along the path of increasing relative humidity map out the equilibrium phase diagram, whereas the collection of conditions that induce transitions in the reverse direction yield the metastability phase diagram. A new stable crystalline phase of $(\text{NH}_4)_2\text{SO}_4 \cdot 4\text{H}_2\text{O}$ is identified. Below $-19.35 \pm 0.05^\circ\text{C}$, the $(\text{NH}_4)_2\text{SO}_4$ anhydrous-ice eutectic point, ammonium sulfate does not deliquesce as the RH is increased but instead undergoes a solid-solid phase transition to form the tetrahydrate phase. $(\text{NH}_4)_2\text{SO}_4 \cdot 4\text{H}_2\text{O}$ incongruently melts at -19.35°C . Equilibrium as well as metastable to stable phase transitions for this system are mapped out. The derived phase diagrams allow for prediction of the composition and phase of $(\text{NH}_4)_2\text{SO}_4$ aerosols under the full range of atmospheric condition and paths. Present observations are in excellent agreement with previous data.

1. Introduction

Atmospheric aerosols play important roles in visibility degradation and climate change¹. Aerosols impact the global climate directly, by scattering a significant portion of the solar radiation to space, and indirectly by controlling cloud optical properties and formation². The largest remaining uncertainty in the estimate of the impact of anthropogenic emissions on climate is the indirect effect of aerosols on cloud coverage and cloud optical properties^{3,4}. For these reasons processes related to atmospheric aerosols have recently taken center stage in atmospheric science research. Aerosols and cloud droplets are also sites for important heterogeneous reaction pathways that alter atmospheric chemistry and composition⁵.

Sulfates are the most important class of anthropogenic atmospheric aerosols. They are the product of the oxidation of SO_2 to H_2SO_4 ^{5,6}. In the remote atmosphere where aerosol concentrations are low, sulfuric acid molecules nucleate to form new particles⁷. In the polluted environment, where particles are abundant, sulfuric acid molecules tend to condense on pre-existing particles. In the lower polluted troposphere, where ammonia concentrations tend to be high, sulfuric acid particles can be neutralized all the way to

ammonium sulfate. At higher altitudes and in the presence of lower ammonia concentrations aerosols may be only partially ammoniated⁸. However, recent experimental results designed to study contrail and cirrus cloud formation show that ammoniated sulfate aerosols can be found even in the upper troposphere as a result of transport by convection⁹.

In this paper we present the ammonium sulfate water phase diagram derived from observations performed on single levitated particles over a broad temperature and vapor pressure range. Droplet growth and evaporation studies of single levitated aerosol particles including $(\text{NH}_4)_2\text{SO}_4$ have been carried out in our laboratory since 1976 by Tang¹⁰⁻¹⁴ et al.. A reproduction of one of these room temperature experiments on $(\text{NH}_4)_2\text{SO}_4$ particles is illustrated in Figure 1 where the particle mass change, resulting from water vapor condensation (open symbols) or evaporation (filled symbols) is expressed as moles of water per mole of solute and plotted as a function of relative humidity (RH). It shows that as RH increases, a solid $(\text{NH}_4)_2\text{SO}_4$ particle remains unchanged (1 to 2) until RH reaches 80%, where it deliquesces spontaneously (2 to 3) to form a saturated solution droplet containing about 9.6 water molecules per solute molecule. Point 2 is the deliquescence point of ammonium sulfate at room temperature. The droplet continues to grow as RH further increases beyond the deliquescence point (3 to 4). Upon evaporation the solution droplet passes the deliquescence point without phase change and becomes a highly supersaturated metastable droplet (4 to 5). Finally, crystallization occurs at 37%RH (5 to 6). Similar results were also reported by Richardson et al. (1984)¹⁵, Rood et al. (1989)¹⁶ Cohen et al.(1987)¹⁷ and Chan et al.(1992)¹⁸.

A low temperature single particle levitation system recently developed in our laboratory allowed us to extend the earlier studies¹⁰ and explore the behavior of this binary system over a much wider temperature range. In this paper, we report the first complete single particle derived $(\text{NH}_4)_2\text{SO}_4 / \text{H}_2\text{O}$ equilibrium and metastability phase diagrams and the discovery of a new low temperature crystalline $(\text{NH}_4)_2\text{SO}_4 \cdot 4\text{H}_2\text{O}$ phase. Section 2 is a brief description of the experimental system, Section 3 illustrates some experimental results. The phase diagrams are given in Section 4 and Section 5 provides some thermodynamic parameters for the saturated solution.

2. Experimental

a. The chamber

Figure 2 is a schematic representation of the low temperature apparatus. The single-particle levitation cell constructed from copper to assure thermal equilibration is suspended inside a vacuum shroud. The cell, is in thermal contact with liquid nitrogen through heat transfer straps (ST). Two resistive heating elements (H) allow for precise temperature control in the range of -140°C to 30°C . This system can be operated in fixed or scanning temperature modes. Temperature of the levitation cell is monitored on the outside; in contact with the cell wall, and inside, above and below the particle (T_m). All the reported data points correspond to conditions in which the two temperatures, above and below the particle are within 0.25°C . The system was calibrated against ice pressure, we estimate the absolute accuracy at $\pm 0.2^{\circ}\text{C}$.

b. The particle trap

A DC potential is impressed symmetrically on the top (t) and bottom (b) sheets of the two- hyperboloidal electrodes. The symmetry of the DC potential is maintained by a series of variable potentiometers over a range up to 20 volts. An AC potential is impressed upon the hyperboloidal conductor (ac). The AC potential varies over a range of 500 volts. Under the proper conditions an electrically charged aerosol particle can be contained for over a week at the null point in space by an alternating electric field, where the particle is balanced against gravity by a DC potential, V_{DC} . The theory and design of the single-particle levitation cell, also known as an electrodynamic balance, have been treated fully by others^{11-14,19-21}.

A charged particle is obtained from a doubly filtered 4%, by weight solution of known composition that is loaded into a particle gun from which a single particle is produced by impact and injected into the trap. The particle is captured in dry nitrogen at the center of the cell by manipulating the AC and DC voltages applied to the electrodes. The diameter of the dry particle is typically between 5 and 10 micrometers. A linear, vertically polarized HeNe laser beam enters the cell through a side window and is focused on the particle at all times. The intensity of the scattered light is continuously monitored at 90 degrees to the laser path. Phase transitions (solid - liquid) are readily detected from the changes in Mie scattering. Since this single-particle levitation system is capable of

operating over a wide temperature range and under controlled gas phase conditions, it provides a very powerful tool for the study of physical and chemical properties of particles under realistic atmospheric conditions.

$(\text{NH}_4)_2\text{SO}_4 / \text{H}_2\text{O}$ particles were generated and captured at -10°C . The system was then closed and pumped to a pressure below 10^{-7} torr. For constant temperature experiments, the chamber temperature was set and the DC voltage (V_0) required to position the dry particle at the null point was noted. V_0 is the voltage corresponding to the mass of pure $(\text{NH}_4)_2\text{SO}_4$ particle. After V_0 was measured, water vapor was slowly introduced into the system and the particle's mass and phase monitored as a function of water vapor pressure.

In the present study we also conducted a set of experiments designed to establish the properties of the system at temperatures and water pressures where the solution is in equilibrium with ice. To explore this part of the phase diagram, $(\text{NH}_4)_2\text{SO}_4$ particles were deliquesced at constant temperature below 0°C , and the water vapor pressure was increased until ice plated on the cell walls. At this point the cell was sealed and the particle composition was measured as the temperature was reduced. This procedure insures that throughout this path the system is maintained at equilibrium with ice.

3. Results

The data reported here is a product of a large number of experiments on many particles. In Figures 3 and 4 we provide an example of two such experiments, one at constant temperature, and, the second a hybrid experiment consisting of a constant temperature hydration followed by a temperature scan along the ice line.

Figure 3 illustrates a hydration/dehydration cycle as a plot of mole ratio $\text{H}_2\text{O} / (\text{NH}_4)_2\text{SO}_4$ vs. relative humidity at a constant temperature of -9.4°C . The cycle shown in this figure is qualitatively very similar to the room temperature cycle shown in Figure 1. In the path 1 to 2 in Figure 3 the particle exists as anhydrous $(\text{NH}_4)_2\text{SO}_4$ which is the stable phase up to a $\text{RH}=82.2\%$ (point 2); the deliquescence RH at -9.4°C . At this point, the particle absorbs water rapidly to form a saturated $(\text{NH}_4)_2\text{SO}_4$ solution droplet (path 2 to 3), containing about 11 water molecules per $(\text{NH}_4)_2\text{SO}_4$ solute molecule. As the RH is increased beyond the deliquescence point the particle takes up water causing the $(\text{NH}_4)_2\text{SO}_4$ concentration to be more dilute (point 4). On the reverse path, where the

RH is decreased, the particle remains in the liquid phase far beyond the deliquescence point to produce a supersaturated solution. The dehydration path (4 to 5) exhibits the typical hysteresis, and from point 3 to 5 is a metastable supersaturated solution. At this temperature (-9.4°C), the efflorescence point (5) is at RH=46% where the particle suddenly transforms into crystalline anhydrous $(\text{NH}_4)_2\text{SO}_4$, shedding all excess water in the process. Note that while the deliquescence point at -9.4°C is only 2.2% different in RH from that at 25°C, the efflorescence RH increases from 37% to 46%.

Figure 4 illustrates a hybrid cycle that was designed to derive the properties of this system along the water ice frost line. This cycle starts with hydration of an anhydrous particle, path 1 to 2, at a constant temperature of -13.5°C. At this temperature the deliquescence point (2 to 3) is at 1.35 Torr (RH=82.4%) and the saturated solution droplet composition is 11.6 water molecules per $(\text{NH}_4)_2\text{SO}_4$ solute molecule. The path 3 to 4 produces a dilute solution at which point the water pressure is slightly below that of ice at -13.5°C. In order to bring the system to the ice frost point the temperature is decreased to -15.8°C while keeping the water vapor source open. This path is labeled by a dashed line to indicate that both temperature and pressure are changing simultaneously in a complex manner (path 4 to 5). This procedure is followed by a waiting period of a few hours to allow the system to reach equilibrium, as noted by constant temperature and water pressure equal to that of ice. At the end of the waiting period the chamber walls are coated with ice and as long as the temperature is not allowed to rise above -15.75°C the water vapor pressure in the cell is equal to and thereafter controlled by the vapor pressure of ice. The temperature dependent composition of the $(\text{NH}_4)_2\text{SO}_4$ solution that is at equilibrium with ice is obtained by measuring the particle mass as a function of temperature, path 5 to 6. As shown in Figure 4, $(\text{NH}_4)_2\text{SO}_4$ particles remain homogeneous super cooled solution droplets down to -33.3°C (6) where they suddenly transform into a solid particle containing approximately five water molecules per ammonium sulfate. Within slightly more than half an hour, at constant temperature and pressure, it loses additional water and attains its final stable composition of $(\text{NH}_4)_2\text{SO}_4 \cdot 4\text{H}_2\text{O}$ (path 6 to 7).

Once formed, the tetrahydrate phase is stable as the temperature is further varied along the ice line up to -19.35°C, as indicated by path 7 to 8. At -19.35°C the particle incongruently melts into the anhydrous phase and its saturated solution. Note that -19.35°C is the eutectic point between ice and the anhydrous phase. It is therefore also the anhydrous deliquescence temperature at ice pressure, which is the water vapor

pressure throughout this experiment. Consequently, the melt composed of anhydrous and its $(\text{NH}_4)_2\text{SO}_4$ saturated solution promptly deliquesces to form a single phase 38.4% $(\text{NH}_4)_2\text{SO}_4 / \text{H}_2\text{O}$ solution (8 to 9). This cycle was found to be perfectly reproducible. We have also observed the melting of the tetrahydrate phase at lower-than-ice pressure at the same temperature of -19.35°C . Under these conditions the melting particle promptly transforms into the anhydrous phase.

The two distinct pathways that the system takes following incongruent melting; at ice and lower-than-ice pressures delineate some of the sharp differences between bulk and particle behavior. In particle form the system must make a choice between a purely liquid state — for pressures equal to or higher than ice, or purely solid state — for pressures lower than ice. In contrast, when a bulk sample of $(\text{NH}_4)_2\text{SO}_4 \cdot 4\text{H}_2\text{O}$ incongruently melts at -19.35°C it produces a mixed phase of an anhydrous precipitate in a saturated solution.

As part of our routine quality assurance, we require that all reported data derive from experiments in which closure was demonstrated. To assure that the data is free from artifacts such as charge loss, or contamination we end the experiment at the starting point. In order to close the cycle presented in Figure 4, melting and deliquescence were followed by a slight increase in temperature to -17.5°C , (9 to 10) and a dehydration at constant temperature, path 10 - 11 - 12. At point 11 the particle effloresces to produce the anhydrous phase at point 12 and the cycle is closed.

The tetrahydrate phase can also be produced via a direct anhydrous to tetrahydrate transition. These experiments are carried out under nonequilibrium conditions in which the temperature is controlled to be less than -19.35°C and the water pressure is momentarily increased above the equilibrium ice vapor pressure. At the point where the water pressure is increased to the expected deliquescence point of the anhydrous phase we observe a phase change. It can qualitatively be described as a partial deliquescence that results in the anhydrous phase absorbing 4 water molecules to form $(\text{NH}_4)_2\text{SO}_4 \cdot 4\text{H}_2\text{O}$.

Once produced and as long as the temperature is kept below -19.35°C the tetrahydrate phase does not transform back to the anhydrous phase even if the pressure is reduced to 10^{-7} torr for several days. This behavior appears to be a common property of aerosols. The general rule is that phase transitions induced by increasing RH take place at equilibrium, and in contrast, the transitions induced by decreasing RH take place far from

equilibrium, from a metastable to stable phase. In particular, the persistence of crystalline hydrates down to water vapor pressures that are many orders of magnitude lower than the equilibrium pressure appears to be commonplace. Similar observations were made in the case of $(\text{NH}_4)\text{HSO}_4 \cdot 8\text{H}_2\text{O}$, and $\text{LiClO}_4 \cdot 1\text{H}_2\text{O}$ ^{22,23}.

The combination of data such as presented in Figures 1, 3, and 4, of the vapor pressures temperatures and compositions where phase transitions occur as the RH is increased yields the complete equilibrium phase diagram. Similarly, the conditions of phase transformations that are induced as the RH is decreased provide the data for the construction of a metastability phase diagram. Both types of phase diagrams are presented below.

4.a. Equilibrium Phase Diagram

Figure 5a shows the $(\text{NH}_4)_2\text{SO}_4 / \text{H}_2\text{O}$ equilibrium phase diagram in the composition temperature domain. The pure solution region is indicated by horizontal lines. The observed deliquescence, points labeled with open circles, define the $(\text{NH}_4)_2\text{SO}_4$ -solution coexistence line. The ice-solution coexistence line down to -33.3°C is labeled with crossed open circles. The data points extending beyond the eutectic point (EU) at -19.35 represent the supercooled solution that is in equilibrium with ice. The tetrahydrate incongruent melting point at -19.35°C is represented by the horizontal line (IM). The dashed line is a qualitative reminder of the presence of a tetrahydrate phase below -19.35°C .

Figure 5b shows the same phase diagram given in Figure 5a, now presented in the water vapor pressure, temperature domain as a plot of $\log(P_w)$ vs. $1000/T$. The symbols in this figure follow those in Figure 5a. Also shown in Figure 5b is the water-ice frost line and the liquid water vapor pressure as functions of $1/T$. The anhydrous deliquescence points form a nearly straight line in this plot.

The observed anhydrous to tetrahydrate solid-solid phase transitions are labeled as checkered squares. These transitions were induced at temperatures below -19.35°C , by rapidly increasing the water pressure to a pressure above that of ice. The data, although not as precise as the rest of the measurements in this study suggest that this transition occurs along the anhydrous deliquescence line. The light scattering pattern during this transition indicates a partial solid to liquid transition that is immediately followed by the

formation of a new solid with a composition consistent with the tetrahydrate. The incongruent melting point (IM) is shown as a vertical line in this representation, and the tetrahydrate stability region lies to the right of this line. It is interesting to note that the hydrated solid forms for both ammonium sulfate and ammonium bisulfate; tetrahydrate and octahydrate respectively form upon cooling a solution droplet along the ice line as well as via solid-solid phase transitions.

4.b. Metastability Phase Diagram

Because phase metastability in aerosols is the “rule” rather than the exception, the phase diagram above is a map in pressure, temperature and composition of the conditions where phase transitions take place as the RH is increased only. Transitions along the path of increasing RH tend to occur at equilibrium. In contrast phase transformations along the reverse path almost always commence from highly metastable states. This is a manifestation of a free energy barrier that must be overcome in order to form the critical nucleus¹¹.

Whether it is useful to construct a map, in pressure, temperature, and composition of the conditions where phase transitions along the path of decreasing RH occur, depends on how reproducible these metastable to stable phase transitions are. In a recent, similar study on the phase transformations of ammonium bisulfate we have shown that in that system metastable to stable phase transitions take place within a very narrow range of reproducible and therefore predictable conditions²². The present experimental results on ammonium sulfate show the very same behavior. The efflorescence transitions take place along well defined lines, repeatedly producing the same phase within a very narrow range of pressures and temperatures. We interpret these observations to be indicative of the sharp onset of nucleation as supersaturation or undercooling is increased beyond the threshold for the first observable nucleation to occur.

By analogy, we construct the $(\text{NH}_4)_2\text{SO}_4 / \text{H}_2\text{O}$ metastability phase diagram, by combining the conditions: temperature, water vapor pressure, and droplet composition where efflorescence transitions take place. The metastability phase diagram in temperature/composition as well as pressure/temperature domains are shown in Figures 6a and 6b respectively (note the scale change between Figures 5b and 6b). The metastable solution region is the gray area, and the metastable solution to anhydrous transitions are labeled by solid triangles. The single path that yielded, by efflorescence, the tetrahydrate

phase was along the water ice pressure line. That efflorescence points are labeled by the diamonds. These comprise all the efflorescence points that can be accessed by our current experimental system. The remainder of the metastable to stable transitions take place under conditions that require the gas phase to be supersaturated with respect to ice formation and these conditions are inaccessible with our current apparatus. The single data point labeled by a star in Figures 6a and 6b, is the well known homogeneous nucleation of water to ice at -38°C . The remaining efflorescence lines are schematic only.

The region defined by the line indicating the incongruent melting point at -19.35°C ($1000/T=3.94\text{K}^{-1}$) marks the stability region of the tetrahydrate. We find that once the tetrahydrate phase is formed and as long as the temperature remains below -19.35°C this phase remains stable for several days even if water pressures are reduced to 10^{-7} torr. This is consistent with our previous observations on $\text{LiClO}_4 \cdot 1\text{H}_2\text{O}$ ¹³ and $\text{NH}_4\text{HSO}_4 \cdot 8\text{H}_2\text{O}$ ²² indicating that the activation barriers to remove water molecules incorporated into a crystal lattice are very high.

Note that at temperature between -19.35 and -38°C within the gray region either one of the phases; metastable solution, ice, anhydrous, or tetrahydrate can be found depending on the path.

Figure 7 Shows the good agreement between present observations and those obtained from past “bulk” experiments²⁴. This agreement provides solid support for the utility of single particle experiments for providing thermodynamic data needed for the construction of such phase diagrams. The advantage that single particle experiments offer is the ability to investigate homogeneous phase transitions free from walls and the effects of impurities. This method also yields, without additional effort the pressure temperature phase diagram. The solid lines in the figure based on a recent empirical model by S. Clegg et. al^{25,26} also exhibit good agreement.

A summary of all observed phase transitions; deliquescence, efflorescence and solid-solid are shown in Figure 8 as a plot of RH vs. temperature. This Figure shows that the $(\text{NH}_4)_2\text{SO}_4$ deliquescence RH changes only slightly with temperature. In sharp contrast, the efflorescence RH is found to be strongly temperature dependent increasing from 36%RH at 30°C to 70% at -33°C . Below we provide the thermodynamic parameters for the $(\text{NH}_4)_2\text{SO}_4$ saturated solution.

5. 4. Thermodynamic properties of the saturated solution

Measurement of the vapor pressure over a saturated solution provides information on the enthalpies of solution. To derive these quantities we follow Tang and Munkelwitz²⁷, where the change in $\ln RH$ with respect to temperature is expressed as:

$$\frac{d \ln RH}{dT} = \frac{x_2}{x_1} \frac{H_s}{RT^2} \quad (1)$$

where x_2 / x_1 is the molar ratio (solute/solvent), and H_s is the integral heat of solution. The molar ratio at the deliquescence point can be expressed as a polynomial in T :

$$x_2 / x_1 = a + bT + cT^2 \quad (2)$$

Substituting Equation 2 into 1 and integrating from a reference temperature T^* we obtain

$$\ln \frac{RH(T)}{RH(T^*)} = \frac{H_s}{R} \left[a \left(\frac{1}{T} - \frac{1}{T^*} \right) - \ln \frac{T}{T^*} - c(T - T^*) \right] \quad (3)$$

T^* is a fixed reference temperature for which we choose $T^*=298.2\text{K}$.

The coefficients in equation 2 are derived from a quadratic fit to the molar ratio, that is obtained from precise measurements of levitated particle weight. A plot of the observed x_2 / x_1 is shown as a function of temperature in Fig. 9 where the solid curve is the quadratic fit to the data the parameters of which are given in Table 1.

Table 1

H_s / R	a	b	c
606.4	-4.59×10^{-3}	4.026×10^{-4}	-1.27×10^{-7}

6. Conclusion

These data provide solid support for the utility of single particle experiments to generate complete and accurate thermodynamic phase diagrams. The first paper in which we have used this approach was ammonium bisulfate, a system for which there was virtually no previous data for comparison. In the present case, the equilibrium phase diagram has previously been well characterized. We find virtually perfect agreement between published bulk data and presently derived equilibrium phase diagram.

The complete temperature dependent phase diagrams of the binary $(\text{NH}_4)_2\text{SO}_4 / \text{H}_2\text{O}$ system have been reported in this paper for the first time. A new low temperature crystalline phase composed of $(\text{NH}_4)_2\text{SO}_4 \cdot 4\text{H}_2\text{O}$ was discovered. Phase transitions, between phases at equilibrium, and those between metastable and stable phase have been mapped out and presented in two types of phase diagrams. On the basis of these phase diagrams and with the knowledge of a path it is possible to predict the phase and composition of any $(\text{NH}_4)_2\text{SO}_4$ aerosol under any thermodynamic condition.

The reproducibility/predictability of metastable to stable phase transition in ultra pure systems is an important issue and has implications in many fields. Thus far, the systems that we have examined: ammonium sulfate, ammonium bisulfate and sulfuric acid all indicate highly reproducible metastable to stable phase transformations lending credence to the utility of metastability phase diagram. It is important to recognize that metastability phase diagrams will be somewhat particle size dependent. Smaller particles will show deeper supersaturations for the same observation times. As we will show in a separate publication, it is possible on the basis of the present study to derive relationships between particle size and nucleation conditions.

We have yet to investigate whether metastable to stable solid-solid phase transitions are predictable. In the two cases presented thus far we searched for a hydrated crystalline to anhydrous transition as the water vapor pressure was decreased and found none. In LiClO_4 we did observe¹³ $\text{LiClO}_4 \cdot 3\text{H}_2\text{O}$ to $\text{LiClO}_4 \cdot 1\text{H}_2\text{O}$ transitions but no systematic study has yet been carried out.

Acknowledgments:

We would like to thank Professor Anthony Wexler for useful discussion

This work was supported by the Department of Energy

References:

1. Baker, M. B. *Science*, **1997**, 276, 1072-1078.
2. Charlson, R. J.; Schwartz, S. E.; Hales, J. M.; Cess, R. D.; Coakley, J. A.; Hansen, J. E.; and Hofmann, D. J. *Science*, **1992**, 255, 423-430.
3. Stephen E. Schwartz; Meinrat O. Andreae; *Science*, **1996**, 272, 1121-1122.
4. Ravishankara, A. R. *Science*, **1997**, 276, 1058-1064.
5. Twomey, S. *Atmospheric Aerosol*, Elsevier Scientific Publishing Dordrecht, New York, **1977**.
6. Jensen, E. J., O. B. Toon, et al., *J. Geophys. Res.*, **1994**, 99, 10421.
7. Collett, J. L.; Bator, A. Jr.; Xin, R.; Demoz, B. B., *Geophys. Res. Lett*, **1994**, 21, 2393-2396.
8. Sheridan, P. J.; Brock, C. A.; Wilson, J. C. *Geophys. Res. Lett*, **1994**, 21, 2587-2590.
9. Tabazadeh, A., *J. Geophys. Res.*, **1997**, submitted.
10. Tang, I. N. *J. Aerosol Sci.*, **1976**, 7, 361.
11. Tang, I. N.; Munkelwitz, H. R. *J. Colloid Interface Sci.*, **1984**, 98, 430.
12. Tang, I. N.; Munkelwitz, H. R. *J. Geophys. Res.* **1994**, 99, 18,801-18,808.
13. Tang, I. N.; Fung, K. H.; Imre, D. G. and Munkelwitz. H. R. *Aerosol Sci. Technol.* **1995**, 23, 443-453.
14. Tang, I. N. *J. Geophys. Res.*, **1997**, 102, 1883-93.
15. Richardson, C. B.; Spann, J. F. *J. Aerosol Sci.*, **1984**, 15, 563-571.
16. Rood, M. J., Shaw, M. A., Larson, T. V., and Covert, D. S., **1989**, *Nature*, 337, 537-539.
17. Cohen, M. D.; Flagan, R. C.; Seinfeld, J. H. *J. Phys. Chem.*, **1987**, **91**, 4563-4574.
18. Chan, C. K.; Flagan, R. C.; Seinfeld, J. H. *Atmospheric Environment*, **1992**, Vol. 26A, No.9 1661-1673.
19. Wuerker, R.F.; Shelton, H.; Langmuir, R.V. *J. Appl. Phys.*, **1959**, 30, No. 3, 342-349.

20. Frickel, R.H.Schaffer, R. E., and Stamatoff, J. B., *National Technical Information Service, Technical Report, ARCSL-TR-77041*, **1978**, Chem. Syst. Lab., Aberdeen Proving Ground, Md.
21. Yong, P. K. Pun, B. K. L., Chan, C. K., Flagan, R. C., and Seinfeld, H., *Aerosol Science and Technology*, **1994**, 20, 275-284.
22. Imre, D. G.; Xu, Jun; Tang, I. N., and McGraw, R. *J. Phys. Chem.*, **1997**, Vol. 101, No. 23, 4191-4195.
23. Imre, D.G.; Xu, Jun; Tridico, A.C. *Geophys. Res. Lett*, **1997**, 24, 69-72.
24. Timmermans Jean. *Physico-Chemical Constants of Binary Systems in Concentrated Solutions*, Interscience Publishers, Inc., New York, **1960**, Vol. 4, 619-625.
25. Clegg, S. L., Brimblecombe, P., *J. Chem. Eng. Data*, **1995**, 40, 1079-1090.
26. Clegg S. L.; Brimblecombe P.; Wexler A. S. *J. Phys. Chem.* **1997**, submitted.
27. Tang I. N. and Munkelwitz, H. R. *Atmospheric Environment*, **1993**, 27A, 467-473.

Figure Captions

Figure 1 Ammonium sulfate growth and evaporation cycle at 25°C, reproduced from (Tang and Munkelwitz¹²). Open symbols designate the growth phase and filled ones evaporation. The growth cycle starts at 1 with an anhydrous ammonium sulfate crystal that remains in that phase up to the deliquescence point 2. 2 to 3 represents the deliquescence process during which the particle absorbs the exact amount of water required to form the saturated solution, in this case 9.56 phase up to 3 where instead of transforming back to the solid phase the particle remains a homogeneous solution all the way to point 5 where it effloresces, suddenly losing all its water to form the starting anhydrous crystal. The region 3 to 5 represents a supersaturated solution.

Figure 2. A schematic representation of the low temperature cell. The particle, shown at the intersection of the two laser beams, is levitated at the center of the electrostatic trap created by the fields generated by the ac electrode (ac) and balanced against gravity by the dc field created between the top (t) and bottom (b) electrodes. The interaction chamber, shown in solid, made of copper, is thermally connected by heat transfer straps (ST) to the liquid nitrogen reservoir (LN₂). Heaters (H) are used to control the temperature that is monitored at three points above below and outside (T_m).

Figure 3. Ammonium sulfate growth and evaporation cycle at -9.4°C. Symbols are identical to those used for the 25°C cycle shown in Figure 1. The deliquescence point 2 at this temperature is slightly higher than that observed at 25°C and the saturated solution is composed of 11 waters for each ammonium sulfate molecule. Note that while the deliquescence RH at this temperature is only ~2% higher than that at 25°C the efflorescence point is 9% higher.

Figure 4 A composite cycle designed to obtain information along the ice solution equilibrium line. The constant temperature growth path, 1 through 4 carried out at -13.5°C is analogous to that shown in Figures 1 and 3. In order to bring the water pressure in the chamber into equilibrium with ice the chamber temperature was lowered down to -15.75°C while keeping the water inlet valve fully open. Constant pressure is indicative of equilibrium with ice and the path 5 to 6 is a cooling cycle along the ice line. At a temperature of -33.3°C, point 6, the solution droplet suddenly transforms to a solid particle containing ~5 waters for each ammonium sulfate molecule. At constant temperature and pressure the composition of this solid changes gradually by losing

water (6 to 7) until it reaches its final tetrahydrate state. The tetrahydrate phase is stable to any further temperature changes until the temperature is increased to -19.35°C where the particle melts and absorbs water to form the homogeneous solution at point 9. In order to close the cycle the temperature was increased to -17.5°C (10) and kept constant there-after while the chamber pressure was decreased. The evaporation cycle 10 to 11 produces an anhydrous crystal by efflorescence (12) and the cycle is complete.

Figure 5a The ammonium sulfate/water equilibrium phase diagram in temperature vs. composition domain. The pure solution region is indicated by the striped region. The ice-solution equilibrium data points are in crossed circles and the anhydrous solution equilibrium points are in open circles. The eutectic point at -19.35°C and 40W% is labeled by EU. The composition of the tetrahydrate phase and its incongruent melting point are shown as well. The dashed line is a qualitative reminder that the below this temperature there is a tetrahydrate equilibrium region which cannot be mapped in the present experiment. All the data points below the eutectic temperature correspond to a metastable - with respect to ammonium sulfate solids - solution at equilibrium with ice.

Figure 5b The ammonium sulfate/water equilibrium phase diagram in $\log(P_w)$ vs. $1/T$ domain. The pure solution region is indicated by striped region. The ice-solution equilibrium data points are in crossed circles and the anhydrous-solution equilibrium points are in open circles. The eutectic point at -19.35°C (3.94 in the figure) and ice pressure is labeled by EU. The region beyond which the tetrahydrate phase can be found is also indicated. The checkered squares are the anhydrous to tetrahydrate transition points.

Figure 6a The ammonium sulfate/water metastability phase diagram in temperature vs. composition domain. The pure solution equilibrium region is indicated by the open striped region while the metastable solution is the gray striped area. The efflorescence points that produced the anhydrous phase are labeled with closed triangles. The single path along the ice line that resulted in the formation of a tetrahydrate particle is labeled by a diamond. Homogeneous ice nucleation from pure water is labeled with the star. The rest of the metastability limits are qualitative.

Figure 6b The ammonium sulfate/water metastability phase diagram in $\log(P_w)$ vs. $1/T$ domain. The pure equilibrium solution region is indicated by the open striped region while the metastable solution is the gray striped area. The efflorescence points producing

anhydrous phase are labeled with closed triangles. The single path along the ice line that resulted in the formation of a tetrahydrate particle is labeled by a diamond. Homogeneous ice nucleation from pure water is labeled with the star. The rest of the metastability limits are qualitative.

Figure 7 A comparison between present data, previously published data, and most recent model, all showing good agreement as far as the saturated solution composition are concerned.

Figure 8 A summary of all observed phase transitions in the binary ammonium sulfate/water system in a RH vs. temperature plot. The deliquescence points form a straight line in this domain and indicate only a slight change in RH with temperature. The checkered squares indicate anhydrous to tetrahydrate solid-solid phase transitions. The efflorescence points in triangles and diamonds show a significant change with temperature from 36% at 34°C to 70% at -33 °C.

Figure 9 A plot of the composition of the saturated solution, in moles of solute per mole of water as a function of temperature. The line is a quadratic fit to the data the coefficients of which are used to derive the heat of solution (see text for detail).

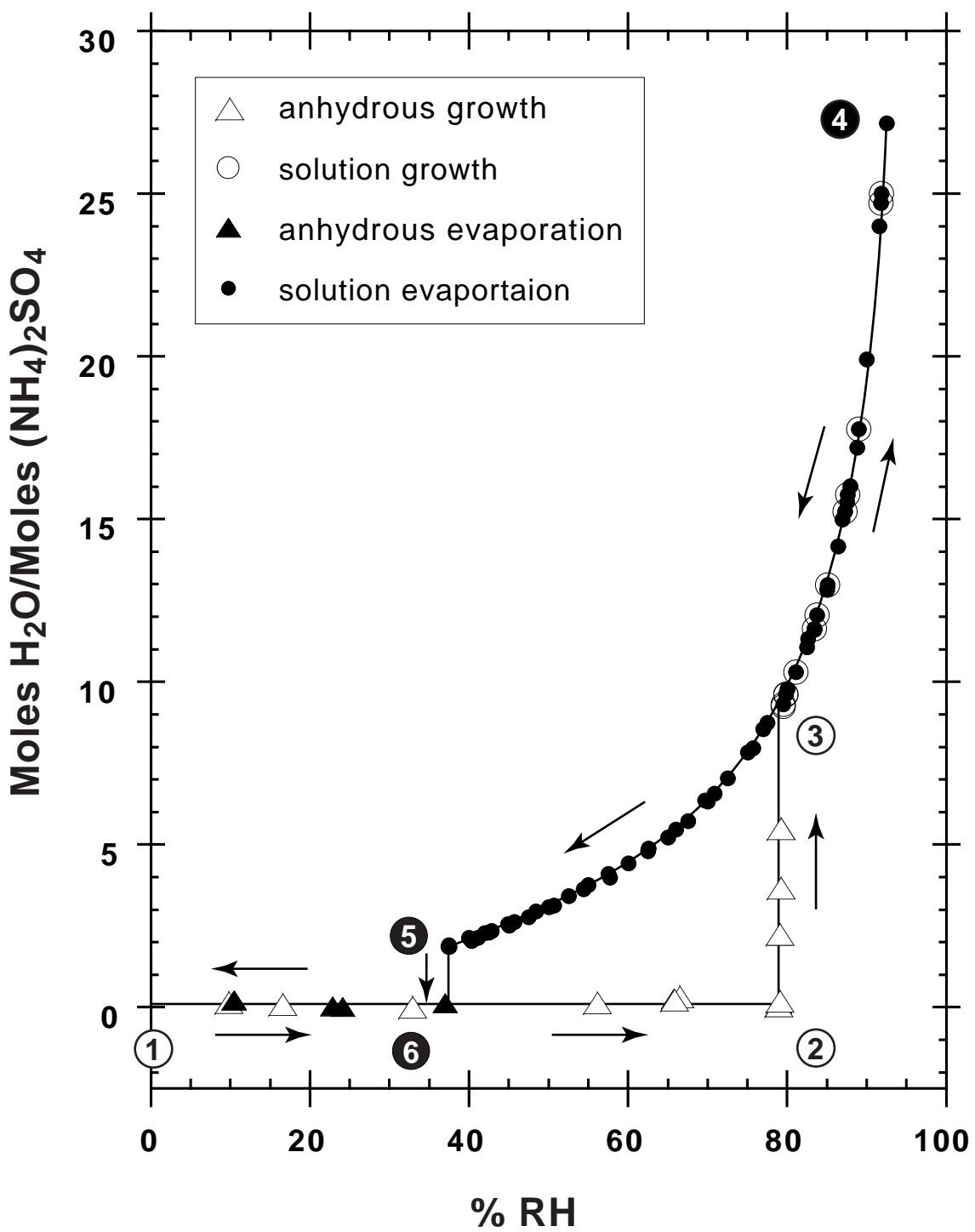


Figure 1

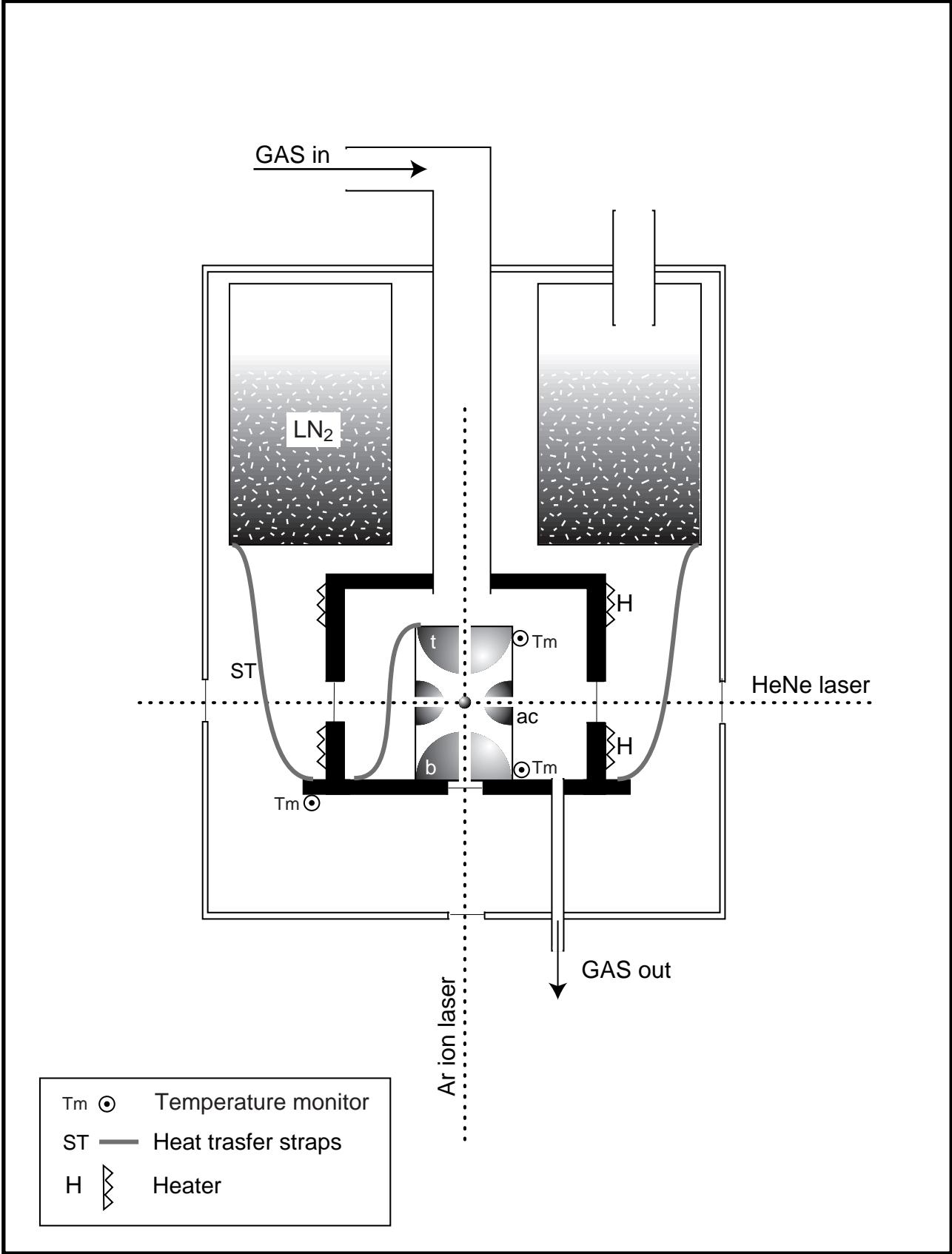


Figure 2

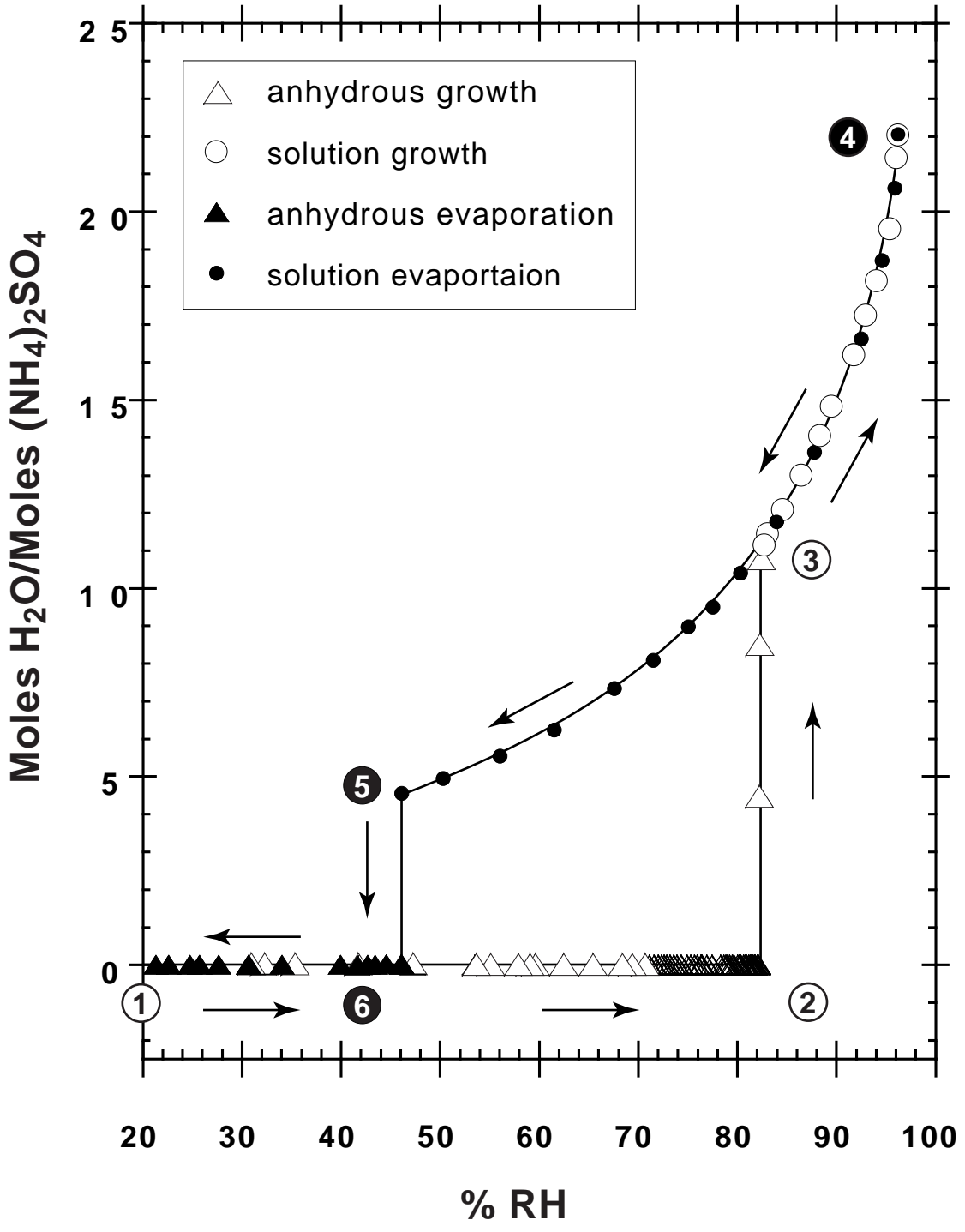


Figure 3

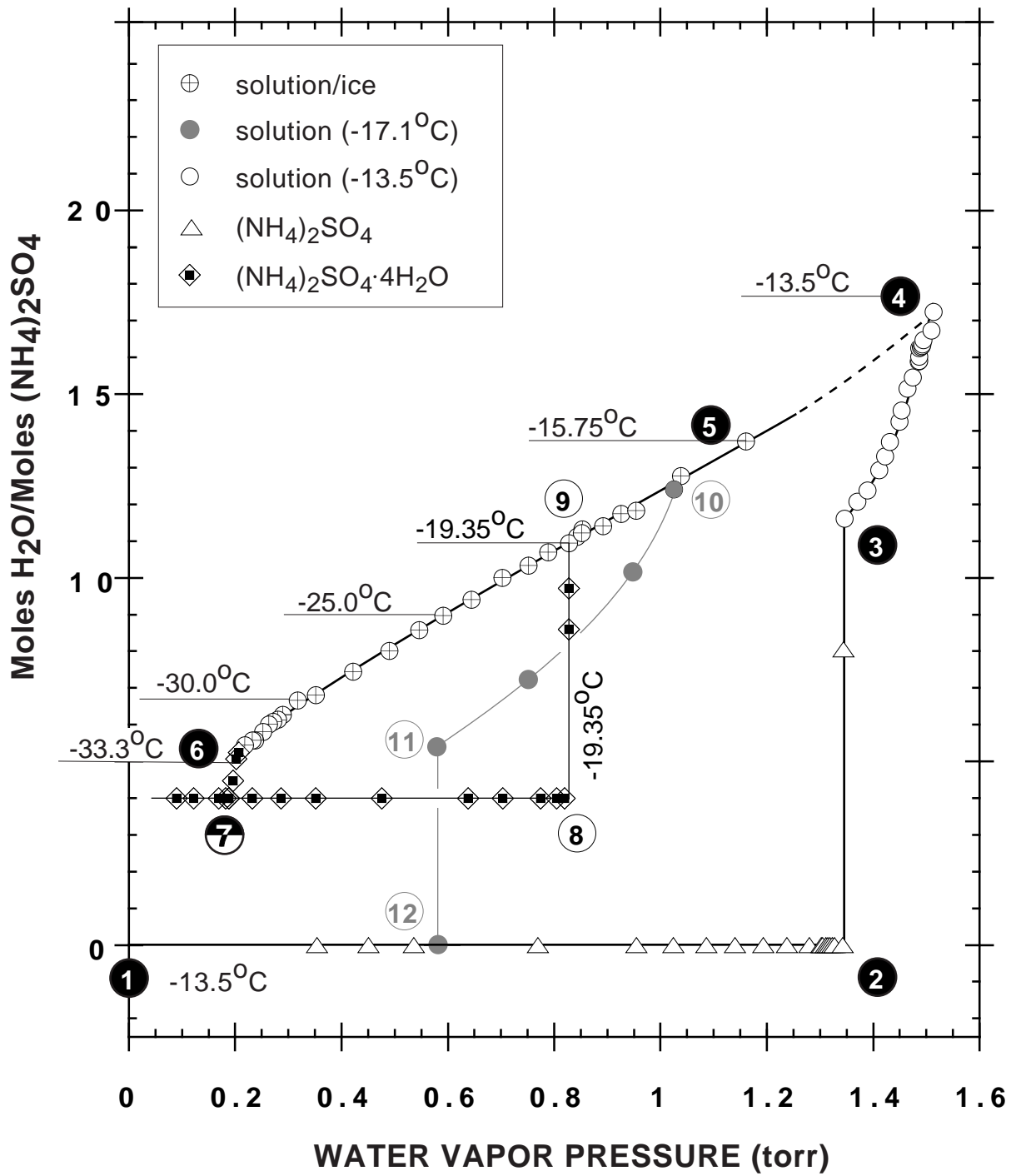


Figure 4

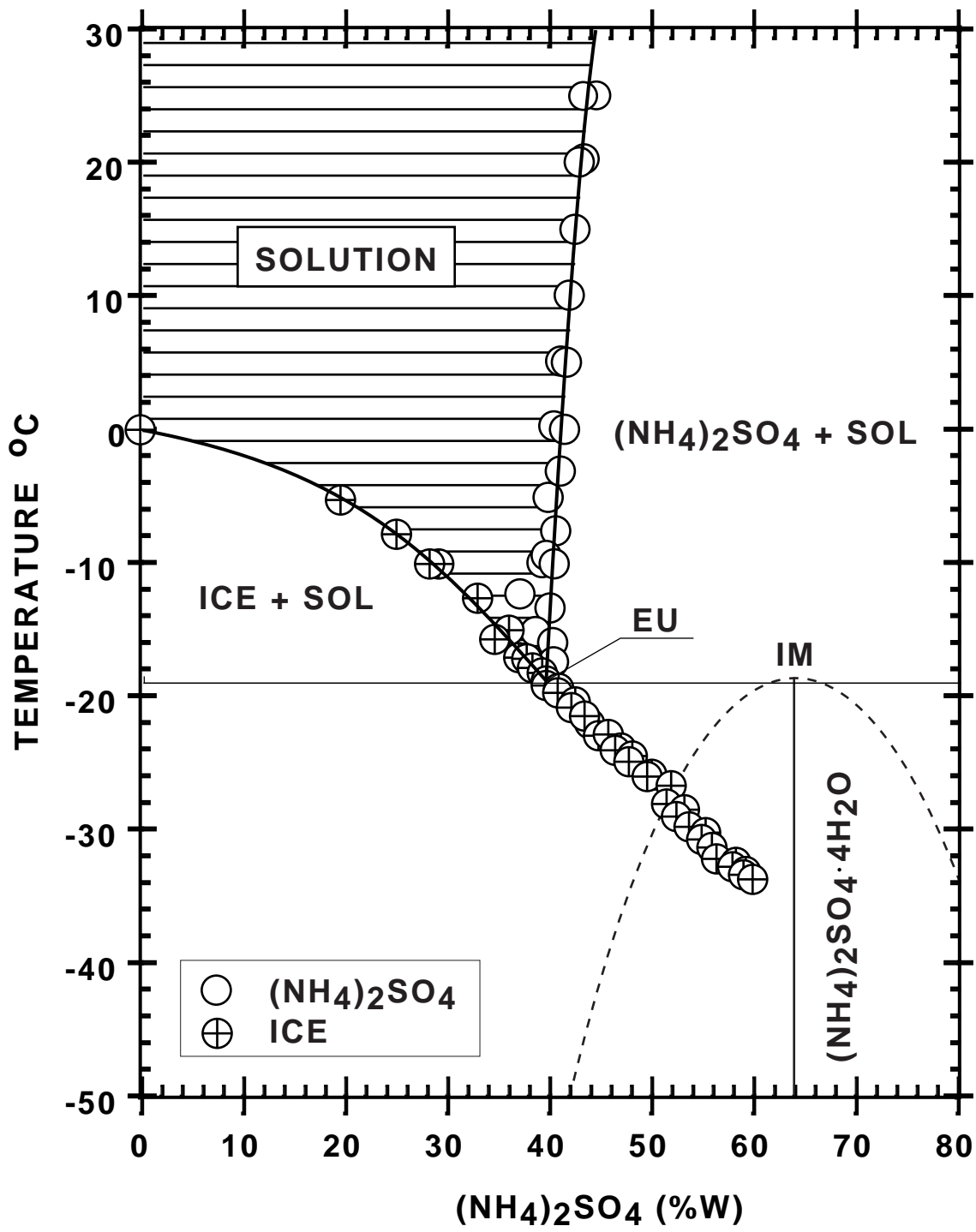


Figure 5a

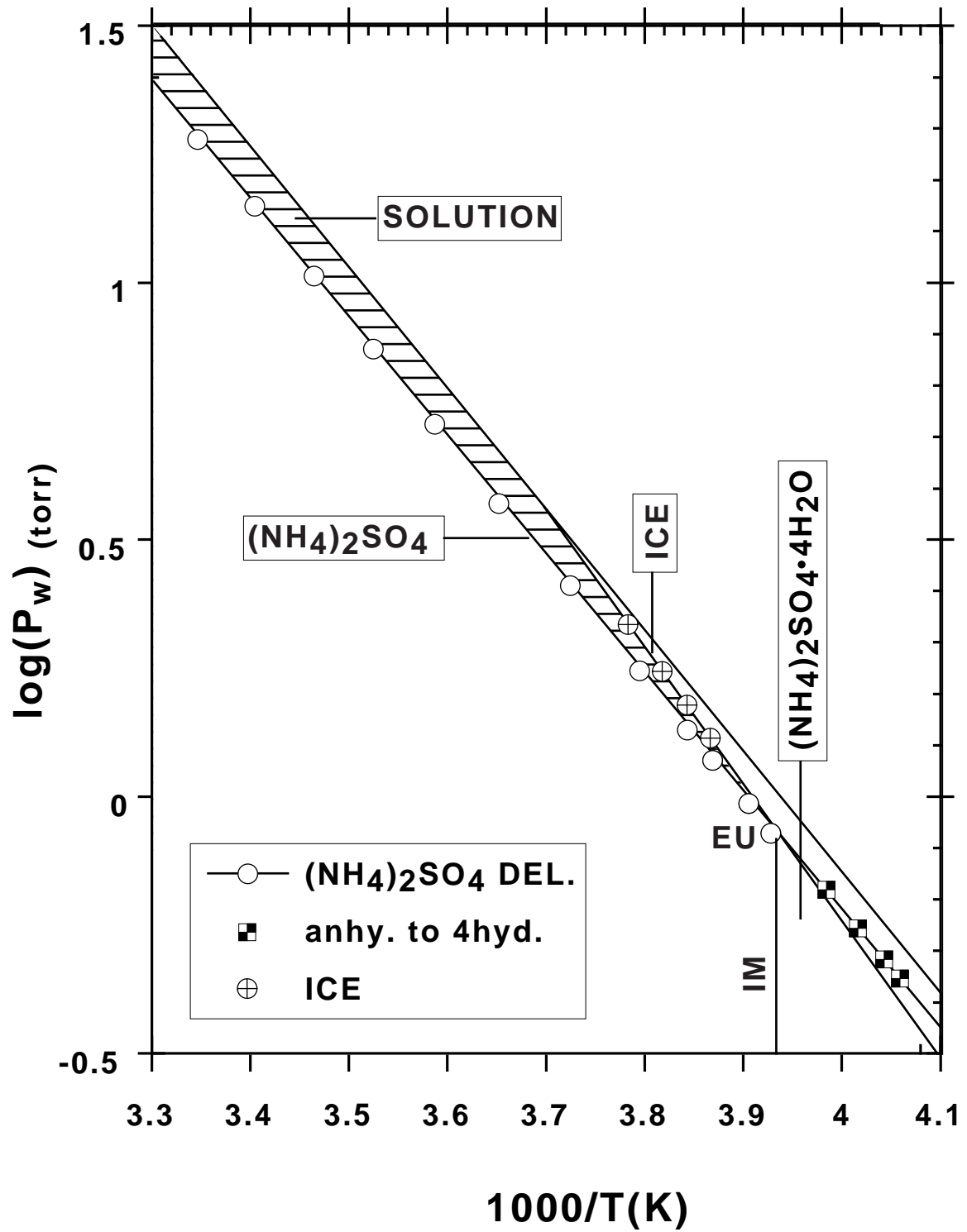


Figure 5b

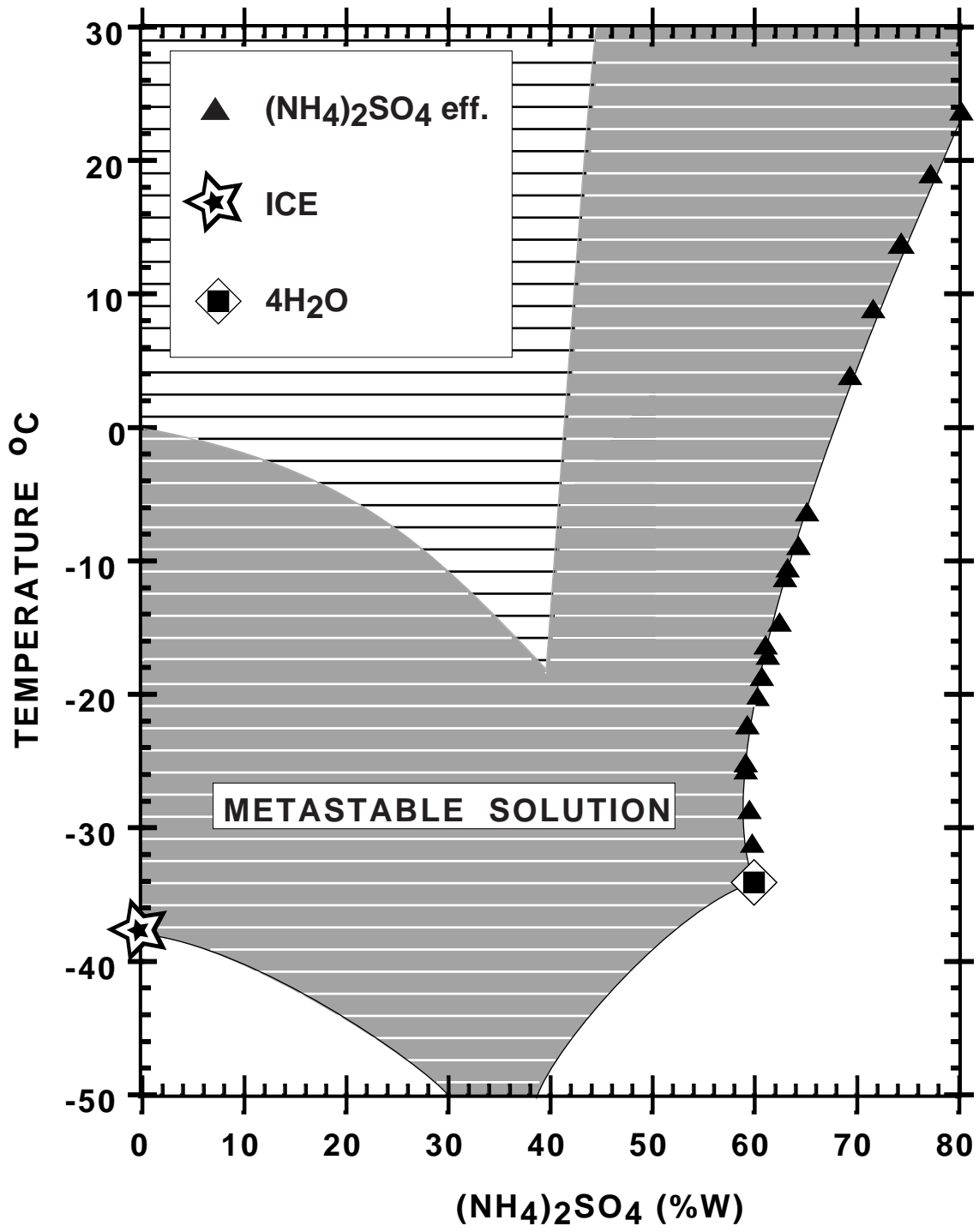


Figure 6a

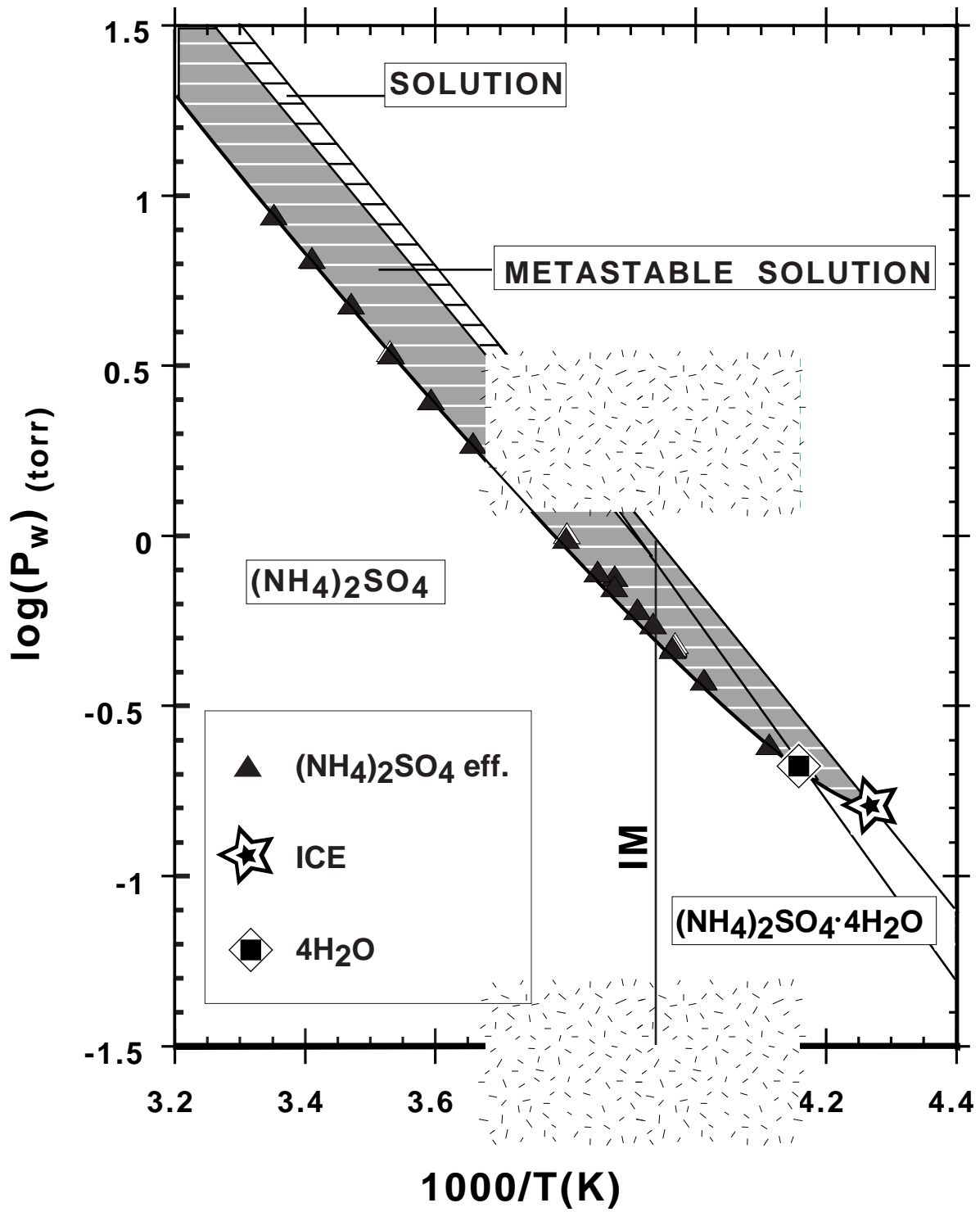


Figure 6b

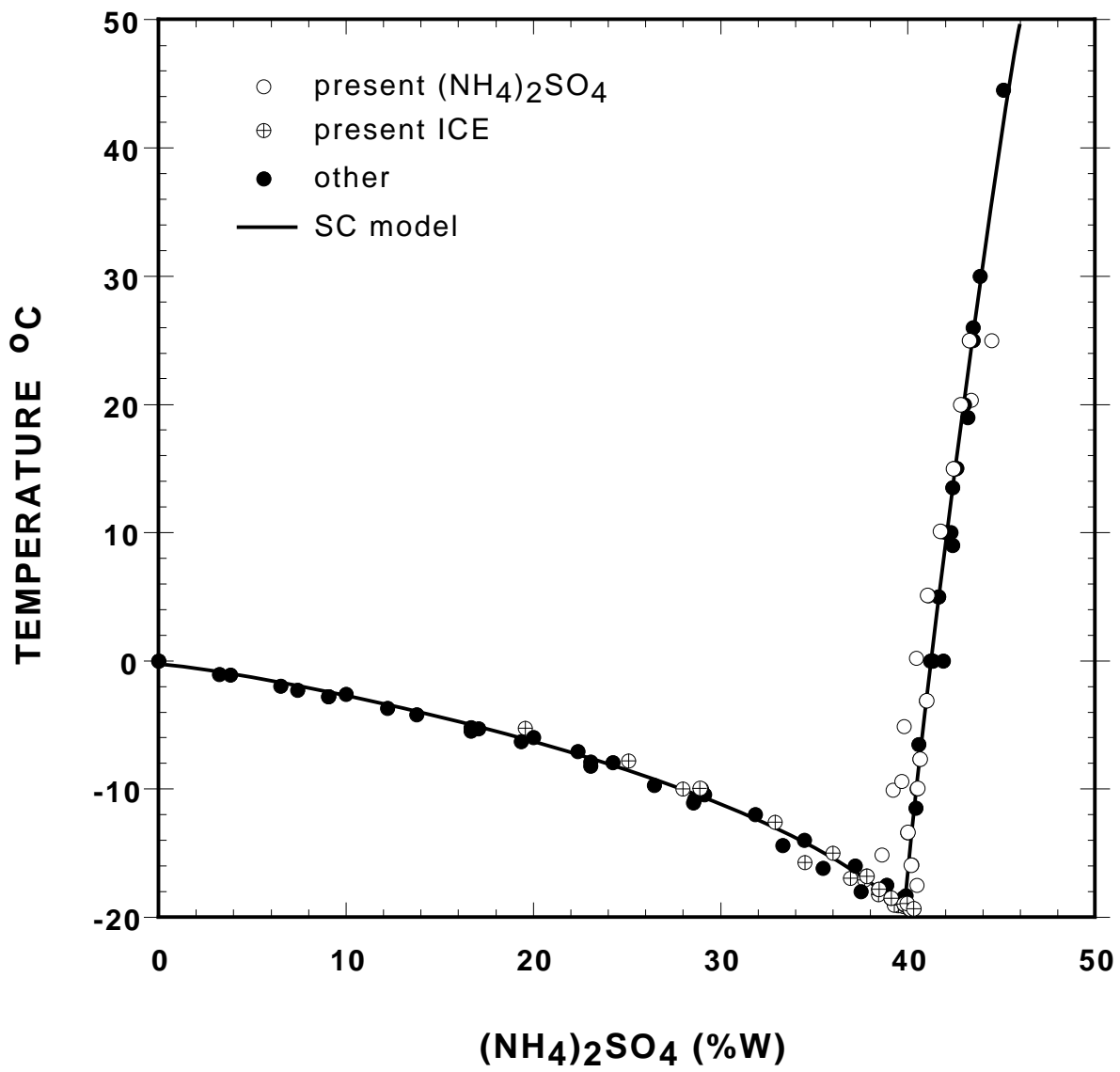


Figure 7

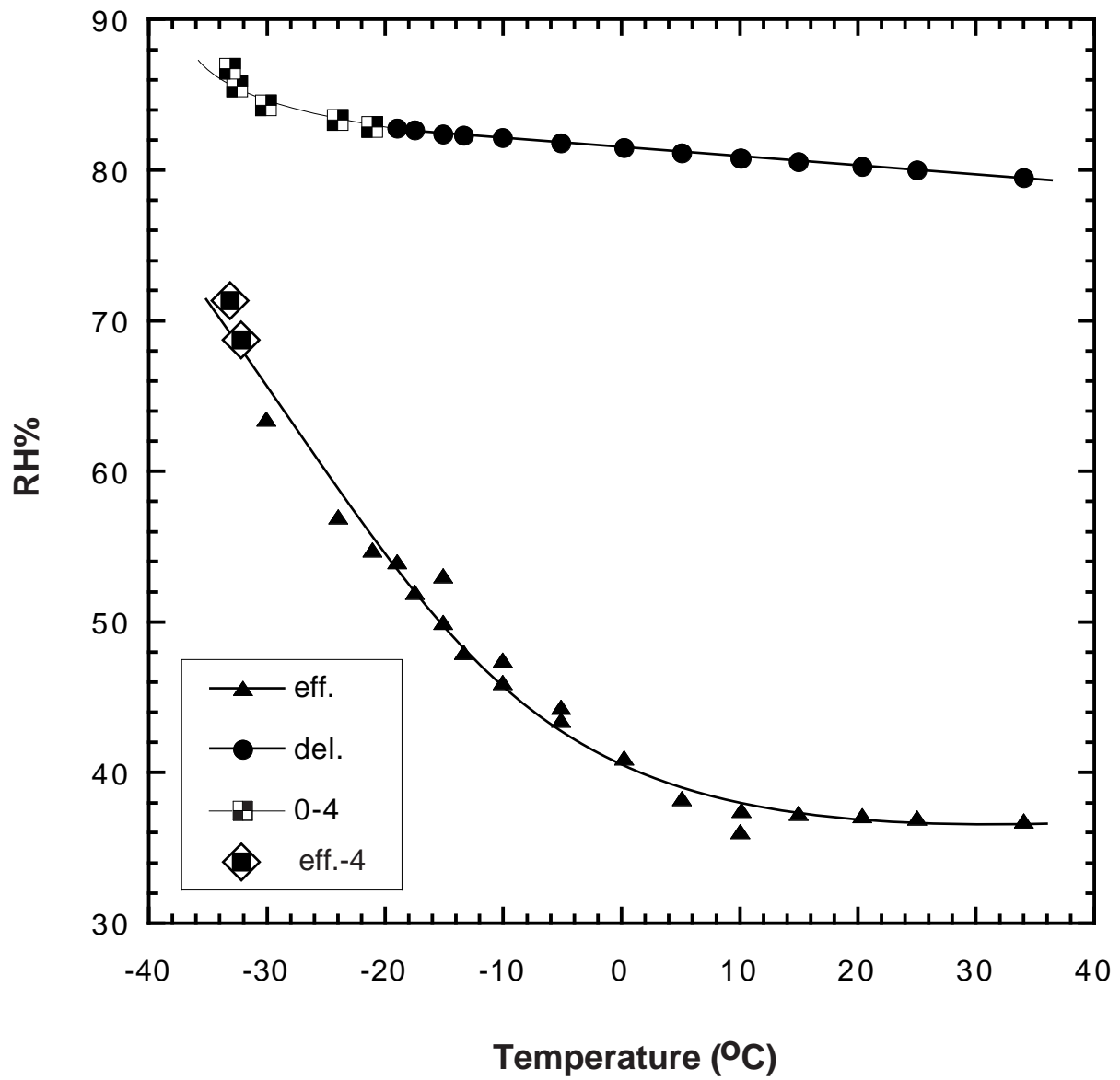


Figure 8

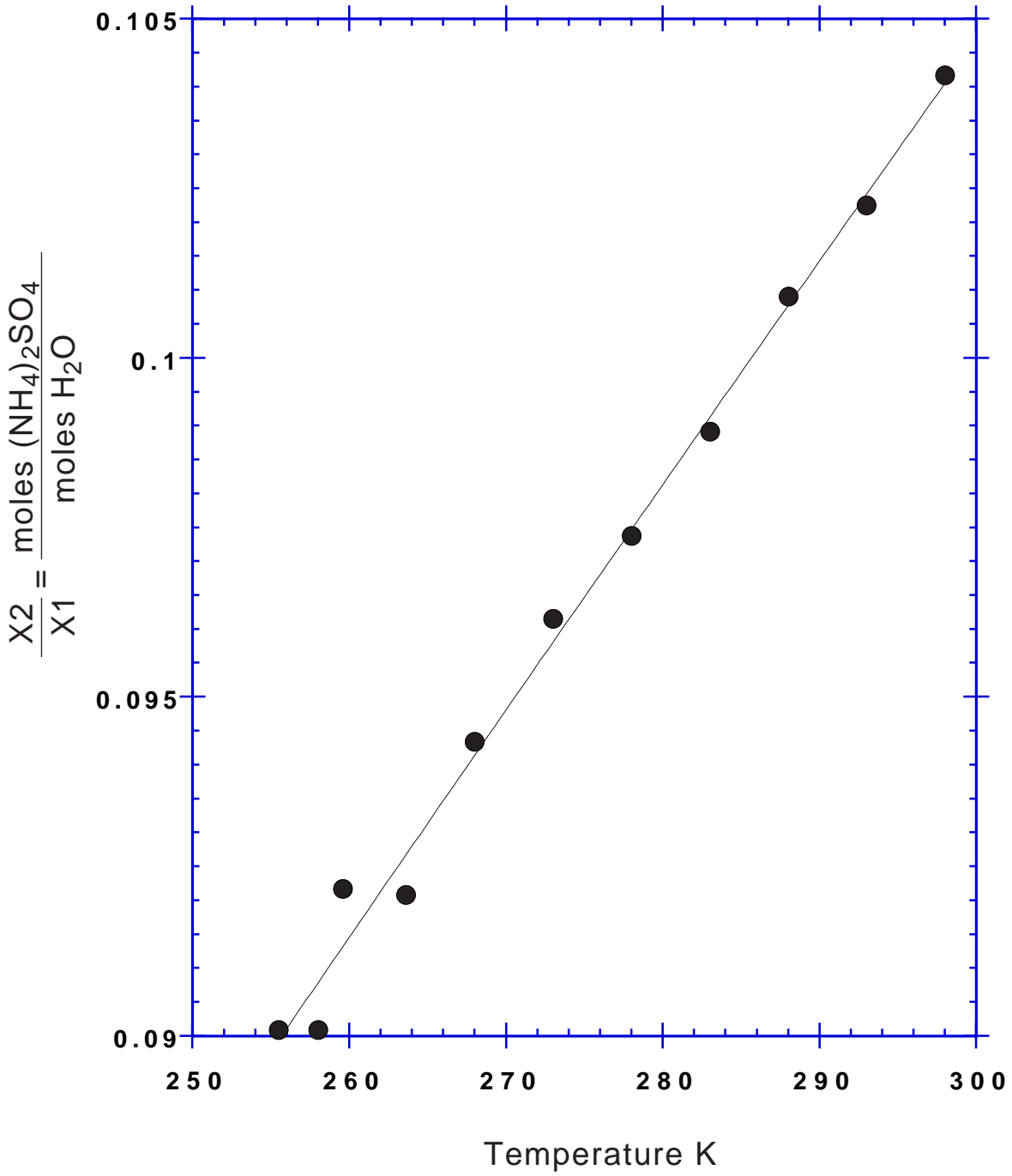


Figure 9